



Cite this: *Nanoscale*, 2023, **15**, 3219

## Atomic layer deposition enables multi-modal three-dimensional electron microscopy of isoporous membranes†

Assaf Simon, ‡<sup>a</sup> Zhenzhen Zhang, ‡<sup>b</sup> Clarissa Abetz, <sup>b</sup> Volker Abetz \*<sup>b,c</sup> and Tamar Segal-Peretz \*<sup>a</sup>

Block copolymers (BCPs) are promising materials for water purification. They enable the fabrication of integral asymmetric isoporous membranes with high permeability and good selectivity. Commonly, the characterization of such hierarchical structures is performed by conventional electron microscopy (EM) means, namely scanning and transmission electron microscopy (SEM and TEM, respectively). However, due to the inherent lack of contrast between BCP domains, external contrast agents are required to achieve informative, high-resolution imaging. In addition, such EM techniques are typically limited to a certain cross-section or surface morphology only. In this paper, we harness the selective growth of  $\text{AlO}_x$  in the pore-forming domains of BCPs to create an internal and stable contrast difference between the blocks. This in turn allowed us to perform advanced three-dimensional characterization of the membranes with focused ion beam (FIB)-SEM and TEM tomography, providing an understanding of the 3D structure and properties such as 3D geometry of the pores, 3D tortuosity, and 3D permeability. This 3D characterization also provides better correlations between the membrane structure and its performance. Such knowledge can allow better design and fine-tuning of BCP membranes and other membranes for their applications.

Received 3rd October 2022,  
Accepted 27th December 2022

DOI: 10.1039/d2nr05477a

[rsc.li/nanoscale](http://rsc.li/nanoscale)

## Introduction

The access, availability, and safety of consumable water is a worldwide concern, as freshwater sources are becoming scarcer, and industrial and agricultural uses result in contamination of readily available consumable water.<sup>1</sup> Filtration membranes play a significant role in addressing this growing demand for clean water due to their ability to separate undesired materials from water.<sup>2</sup> The performance of such membranes depends mainly on properties such as pore size and distribution, porosity, mechanical properties, *etc.*<sup>3</sup> Ultrafiltration (UF) membranes are extensively used for the separation of nanoscale materials (*e.g.* viruses, particles, and bacteria) and as pre-treatment process prior to reverse osmosis (RO) desalination.<sup>4</sup>

The growing demand for high-performance membranes has led to the development of block copolymer (BCP) based membranes.<sup>5,6</sup> For this purpose, BCP self-assembly combined with non-solvent induced phase separation (SNIPS), a robust method for fabricating BCP membranes, was developed in the past decade and a half. SNIPS combines the self-assembly of BCPs and non-solvent induced phase separation,<sup>7</sup> resulting in one integral but asymmetric membrane, with ordered pores at the top of the membrane and a sponge-like, mechanically robust support layer at the bottom of the membrane. SNIPS membranes are fabricated by creating micron thick BCP films, followed by short solvent evaporation which induces the organized self-assembly at the top of the film. The film is then immersed in a non-solvent bath to promote the phase separation and formation of a porous structure. The resulting membrane has a high pore number density, a narrow pore size distribution, low defectivity, and a mechanically stable integral asymmetric structure.<sup>7,8</sup>

An array of BCP materials for SNIPS membranes have been investigated to tune the pore size, functionality, and membrane mechanical and thermal properties. The most common among them is the diblock copolymer poly(styrene)-*b*-poly(4-vinyl pyridine) (PS-*b*-P4VP).<sup>9</sup> Other BCPs either possess diverse thermally stable blocks (*e.g.* poly(*tert*-butyl styrene), poly(4-trimethylsilyl

<sup>a</sup>Department of Chemical Engineering, Technion, Haifa-3200003, Israel.  
E-mail: [tamarps@technion.ac.il](mailto:tamarps@technion.ac.il)

<sup>b</sup>Helmholtz-Zentrum Hereon, Institute of Membrane Research, Max-Planck-Str.1, 21502 Geesthacht, Germany. E-mail: [volker.abetz@hereon.de](mailto:volker.abetz@hereon.de)

<sup>c</sup>Universität Hamburg, Institute of Physical Chemistry, Martin-Luther-King-Platz 6, 20146 Hamburg, Germany

†Electronic supplementary information (ESI) available. See DOI: <https://doi.org/10.1039/d2nr05477a>

‡These authors equally contributed to the paper.



styrene)<sup>10</sup> or polar blocks<sup>11</sup> (e.g. poly(acrylic acid),<sup>12,13</sup> poly(2-hydroxyethyl methacrylate)<sup>14</sup>), or implement the usage of triblock copolymers, e.g. poly(isoprene)-*b*-PS-*b*-P4VP.<sup>15,16</sup> In addition, strategies such as blending BCPs with different molecular weights and compositions,<sup>17</sup> adding additives,<sup>18</sup> or post-modification of pore-forming blocks<sup>19</sup> have added more degrees of freedom in pore size control, while post-modifications<sup>20–22</sup> also enabled additional pore functionality.

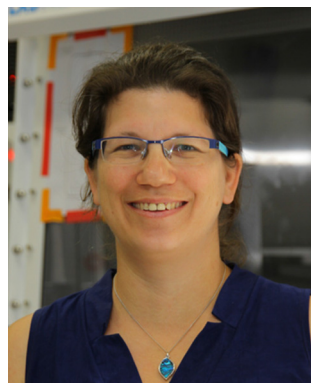
In SNIPS membranes as well as in other filtration membranes, electron microscopy is a central tool for characterizing and studying the membrane structure and correlating between the nanoscale structure and the membrane's performance.<sup>17,23–25</sup> Typically, scanning electron microscopy (SEM) is used to probe the surface properties, such as the pore size and its distribution, and the membrane's cross-sectional morphology.<sup>26</sup> Transmission electron microscopy (TEM) is often used to observe the membrane at high magnifications, allowing insights into the pore morphology.<sup>27</sup> However, moving beyond 2D imaging (surface and cross-sectional) to probing the 3D structure of the membrane is essential for fully understanding the polymer physics that governs the assembly of the membranes and for creating better structure–performance correlations that include the tortuous, connected, 3D pores and pathways. This 3D knowledge is expected to lead to better membrane design and functionality.

Generally, electron microscopy (EM) imaging of polymer-based structures has several challenges. Most polymers are sensitive to the electron beam, and as a result, radiation damage such as scission and cross-linking occurs, which can be destructive to the specimen and impair the ability to reliably image the structure.<sup>28</sup> To overcome the radiation challenge, imaging of polymer-based structures is typically per-

formed using a low electron dose (typically  $\sim 20 \text{ e}^- \text{ \AA}^{-2}$  or lower).<sup>29,30</sup> This may lead to low signal-to-noise images. In addition, the imaging contrast can impose an additional challenge. The main mechanism of contrast of soft matter depends on variations in mass and topography (SEM) and mass-thickness (TEM). Thus, elements that are similar in atomic number or specimens that have a uniform thickness and topography will result in low contrast images. SNIPS membranes are commonly composed of light elements, leading to low contrast between the blocks and between the BCP membrane and the epoxy filling that is often used for TEM cross-sectional specimen preparation. Therefore, external staining agents are commonly used to enhance the contrast in BCP samples, in particular for TEM imaging.<sup>31</sup> For example, for PS-*b*-P4VP SNIPS membranes, iodine is used to selectively stain the P4VP pore-forming block.<sup>32</sup> However, such staining tends to fade over time and might not be stable during long image acquisition methods. Other methodologies for contrast enhancement involve chemical or physical modifications and/or etching.<sup>33</sup> For 3D imaging, it is desired to have high contrast imaging and stable specimens.

Recently, we demonstrated the ability to selectively grow  $\text{AlO}_x$  in the P4VP domains of SNIPS membranes.<sup>34</sup> This was performed using sequential infiltration synthesis (SIS), an atomic layer deposition (ALD) based method, in which gaseous precursors diffuse into the polymer and interact with it, leading to the growth of inorganic materials within the polymer. SIS can be harnessed to create hybrid organic–inorganic materials for applications such as anti-reflective coatings<sup>35</sup> and batteries.<sup>36</sup> If desired, SIS can be followed by the removal of the polymer template, resulting in inorganic nanostructures with high fidelity, e.g. membranes,<sup>37</sup> nanorods,<sup>38</sup> and nanoparticles.<sup>39</sup> SIS selective growth in one BCP domain is typically induced by Lewis acid–base precursor–block interactions.<sup>40</sup> For example, the preferred interactions between trimethyl aluminum (TMA) and the pyridine group led to the selective growth of  $\text{AlO}_x$  within the P4VP domains of PS-*b*-P4VP membranes.<sup>34</sup> The SIS process in these membranes led to the pore size and pore wall composition alteration. Additional pore size reduction and creation of  $\text{AlO}_x$  pore walls that are susceptible to further modifications were achieved with additional ALD cycles.

Here, we investigate how the combination of SIS and ALD can be used to enhance the imaging contrast of SNIPS membranes and enable 3D characterization in both SEM and TEM. The selective growth of  $\text{AlO}_x$  in the P4VP pore-forming domain can achieve an inherent and stable contrast between the blocks over time and temperature, thanks to the higher atomic number of Al and the covalent bond that is formed between Al and the pyridine group during the SIS process. This allowed us to perform high contrast and stable 3D characterization using advanced EM techniques, namely, focused ion beam assisted SEM tomography (FIB-SEM tomography) and TEM tomography. These complementary techniques enabled us to achieve a deeper understanding of the membranes' 3D structure and correlate it with their performance.



**Tamar Segal-Peretz**

*Tamar Segal-Peretz is an Associate Professor at the Wolfson Department of Chemical Engineering, Technion-Israel Institute of Technology. She received her PhD from the Technion, followed by a Director's Postdoctoral Fellowship at Argonne National Laboratory and the Pritzker School for Molecular Engineering at the University of Chicago. Tamar Segal-Peretz's group, the Functional*

*Nanostructure and Advanced Imaging (FNAI) lab, focuses on understanding and developing new functional nanostructures for nanofabrication processes, water technologies, and energy devices using polymer self-assembly and inorganic materials growth within polymers. The FNAI group utilizes and develops various 2D and 3D electron microscopy characterization techniques to probe nanostructures.*



## Experimental details

### Materials and methods

BCP synthesis, membrane fabrication, SIS and ALD processes were all performed as described in our previous paper.<sup>34</sup> Briefly, PS-*b*-P4VP with the desired molecular weight and composition was synthesized by living anionic polymerization in tetrahydrofuran (THF). Membranes were produced by SNIPS in a solvent mixture of THF/*N,N*-dimethylformamide (DMF) and water as the non-solvent. Finally, modification with AlO<sub>x</sub> was done by SIS and ALD. An SIS cycle consisted of 15 ms TMA pulse/300 s hold/350 s N<sub>2</sub> purge/15 ms water pulse/300 s hold/350 s N<sub>2</sub> purge. An ALD cycle consisted of 15 ms TMA pulse/10 s hold/10 s N<sub>2</sub> purge/15 ms water pulse/10 s hold/10 s N<sub>2</sub> purge. We decided on 3 cycles of SIS, based on our previous research, where we concluded that 3 cycles are sufficient to ensure full coverage of the membrane by AlO<sub>x</sub>, while additional 25 or 75 ALD cycles proved the most efficient in reducing the pore size.<sup>34</sup>

### Characterization

The membrane morphology was investigated by SEM and TEM. SEM images were taken on a Merlin (ZEISS, Oberkochen, Germany) at a voltage of 1.5 kV. Cross-sectional SEM samples were prepared by Ar-ion milling (Precisions Etching and Coating System PECS II, Gatan Inc., USA), followed by coating a 4 nm thick layer of carbon on the obtained cross-sections with the same device.

FIB-SEM tomography was performed using a ZEISS Crossbeam 350 (ZEISS, Oberkochen, Germany) with an FE-SEM column and Ion-sculptor focused ion beam (FIB) column. Membranes were milled using the FIB at low currents with a pixel size of 2 nm and a slice thickness of 5 nm. A series of section images (*i.e.*, 660–1800 images) was obtained using the Zeiss Atlas 3D package, in order to ensure precisely known slice thicknesses for permeability and tortuosity evaluation. During the collection of the imaging datasets, the FIB (30 kV/3 nA) and the SEM beam (1.4 kV, 30 μm aperture) were operated simultaneously. The series of slice images was then aligned and reconstructed into a 3D volume using Thermo-Scientific Inspect 3D software. The reconstructed volume was processed and analyzed using FEI Amira 6.4 Software. Pore network model analysis of FIB-SEM tomography was analyzed using the Xpore module of FEI Amira. More detailed information on this process can be found in the ESI.†

TEM images were taken on a Talos 200C field-emission gun equipped transmission electron microscope (Thermo Fisher Scientific, USA) with an acceleration voltage of 200 kV in the bright-field mode. Cross-sectional TEM samples were produced by embedding the membrane samples in an epoxy resin (EPO-TEK®) followed by preparing ultrathin slices (~150 nm) using a Leica Ultra-microtome EM UCT system (Leica Microsystems, Wetzlar, Germany), with a diamond knife (Diatome Ltd, Switzerland). TEM tomography images were obtained using  $\alpha$ -tilts ranging from  $-65^\circ$  to  $65^\circ$  at intervals of  $2^\circ$ . The tilt-series images were then aligned and reconstructed

into a 3D volume using Thermo-Scientific Inspect 3D software. The reconstructed volume was processed and analyzed using FEI Amira 6.4 Software.

## Results and discussion

### The role of AlO<sub>x</sub> growth in SNIPS PS-*b*-P4VP membranes

The main mechanism of contrast in our BCP system is atomic number based, as previously discussed. Since PS-*b*-P4VP contains only light elements, *i.e.* hydrogen, carbon, and nitrogen, and the latter two elements are subsequent in atomic number, a poor contrast between the P4VP pore-forming block and the PS matrix block is expected. This is demonstrated in Fig. 1a and b, showing the cross-sectional SEM (Fig. 1a) and TEM (Fig. 1b) images of a pristine membrane. In the backscattered electron (BSE) SEM image (Fig. 1a), the highly ordered self-assembled top layer cannot be resolved due to the lack of contrast. The contrast challenge is also observed in the TEM image (Fig. 1b), where it is hard to distinguish between the PS matrix block and the P4VP pore-forming block. However, by performing 3 cycles of AlO<sub>x</sub> SIS followed by 25 cycles of ALD, a drastic improvement in the contrast between the two blocks is observed in both SEM and TEM images (Fig. 1c and d, respectively). This drastic improvement is due to the selective growth of AlO<sub>x</sub> inside the P4VP domains. The importance of the initial 3 AlO<sub>x</sub> SIS cycles prior to growth by ALD was discussed in our previous paper, where we demonstrated that the hybrid P4VP + AlO<sub>x</sub> interface created by SIS enhanced AlO<sub>x</sub> growth during the following ALD process.<sup>34</sup>

The heavier Al atoms, which scatter more electrons, enabled us to obtain BSE images with good contrast and thus observe the channels with higher details (Fig. 1c). Noticeably, AlO<sub>x</sub> (lighter regions of the image) covers the whole pore circumference, allowing us to distinguish between the pore walls (P4VP + AlO<sub>x</sub>), the surrounding matrix (PS), and the pores throughout the cross-section. The AlO<sub>x</sub> SIS and ALD also improved the TEM imaging contrast (Fig. 1d), where the pore channels are observed with higher clarity. The Al regions scatter more electrons and therefore appear darker in bright field (BF) TEM. Once again, we can notice a full coverage of the pore-forming P4VP by AlO<sub>x</sub>, allowing us to image the cross-section with higher clarity, contrast, and resolution. Therefore, we can further probe the 3D structure of our membranes in multi-modal EM, namely, FIB-SEM tomography and TEM tomography, as illustrated in Fig. 2. These complementary techniques allowed us to achieve a deeper understanding of the membrane's 3D structure and learn about the correlation of structure–performance.

### FIB-SEM tomography

Our first approach to understanding the 3D structure of the membranes was FIB-SEM tomography. We started by comparing the results from three membrane series: the pristine membrane (Fig. 3a, d and g), the membrane modified with 3 cycles of AlO<sub>x</sub> SIS and 25 cycles of AlO<sub>x</sub> ALD, henceforth denoted as 25A (Fig. 3b, e and h), and the membrane modified with 3 cycles of AlO<sub>x</sub> SIS and 75 cycles of AlO<sub>x</sub> ALD, henceforth





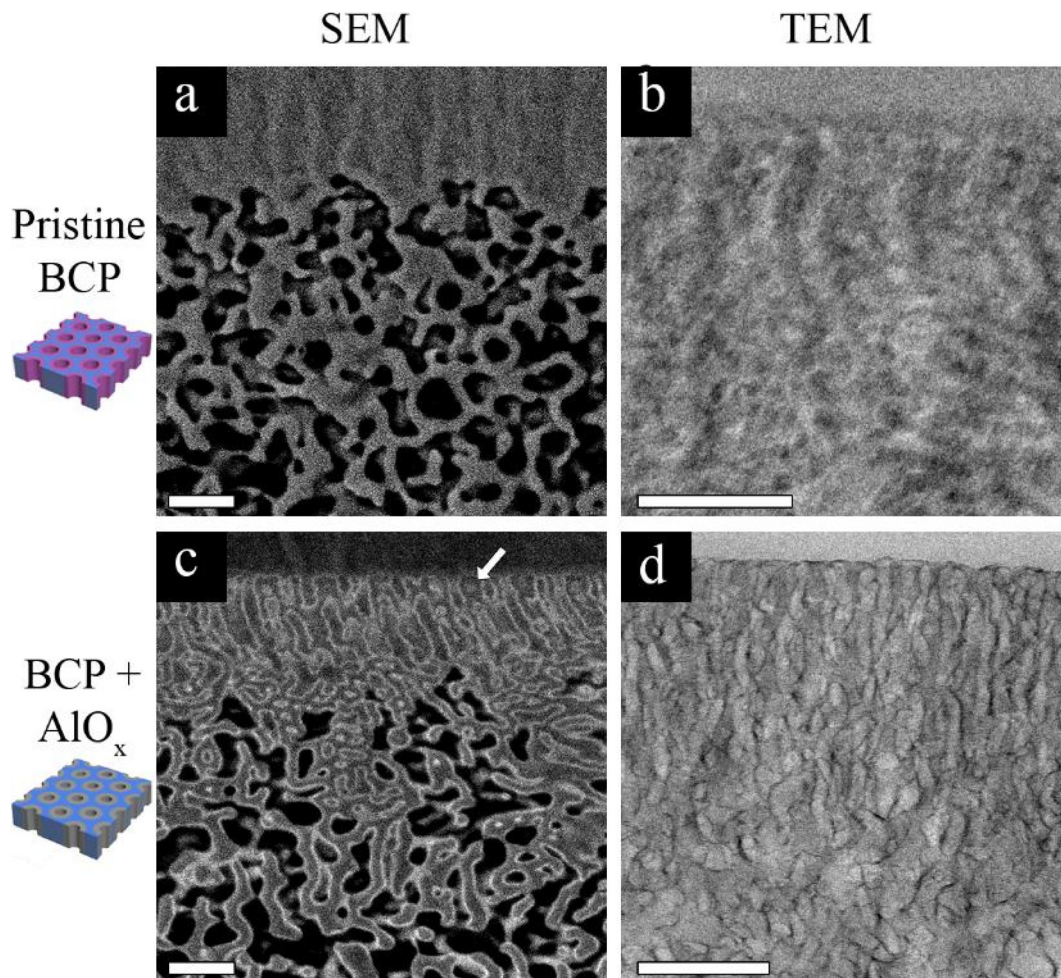


**Fig. 1** Cross-sectional EM images. (a) BSE-SEM of a pristine membrane and (b) its corresponding TEM (b); (c) BSE-SEM of a membrane modified with  $\text{AlO}_x$  by SIS and ALD (the white arrow point to the top surface) and (d) its corresponding TEM. All the scale bars are 200 nm.

denoted as 75A (Fig. 3c, f and i). The first two rows show cross-sectional SEM images with a lower magnification (Fig. 3a–c) and a higher magnification (Fig. 3d–f). The pristine membrane (Fig. 3a and d) shows a very poor contrast between the blocks. Moreover, the highly ordered self-assembled layer (black arrows) is barely visible in the cross-section, making it hard to visualize the interface between the selective and supporting layer (white arrows) and to characterize the selective layer (Fig. 3a). The modified membranes containing  $\text{AlO}_x$ , on the other hand, show an improved contrast. We can clearly distinguish between the BCP matrix and pore channels. Also, the interface between the selective and supporting layers is well defined (Fig. 3b, c, e and f). The effect of the additional ALD cycles is mainly pronounced in the selective layer. The pore channels of the selective layer are better defined in the 75A samples compared to 25A, as we can see additional details of the pore structure and better visualize the interface between the selective and supporting layers (Fig. 3e and f).

The effect of  $\text{AlO}_x$  is even more pronounced in 3D volume reconstruction (Fig. 3g and i). We can barely notice any details in the pristine membrane. The interface between the layers is

almost non-visible and the pores are hard to distinguish. In both samples with  $\text{AlO}_x$ , on the other hand, we can observe the well-ordered surface pores, the distinct interface between the layers, and distinguishable pore channels. Such a contrast allowed us to further analyze the pore network system in 3D volume.

We chose to focus on the 75A membrane for pore network analysis since the significant  $\text{AlO}_x$  growth in this membrane enabled clear imaging of the highly ordered selective layer with a distinct interface between the selective and supporting layers. To analyze the 3D pore network, we started by segmenting the 3D data into pore channels and the polymer matrix (Fig. 4a). The good fit between the segmented and original data in their overlay (Fig. 4b) indicates the reliability of the threshold algorithm. The complete 3D segmented data (Fig. 4c) together with the good segmentation agreement show that we can analyze our membrane's pore network throughout a high depth range ( $\sim 1.8 \mu\text{m}$ ).

The segmented data are then analyzed by a 3D pore network model, using the xPore algorithm in Amira®. This analysis enables us to model the flow of liquid through the membrane pores, with a transmembrane pressure drop. The





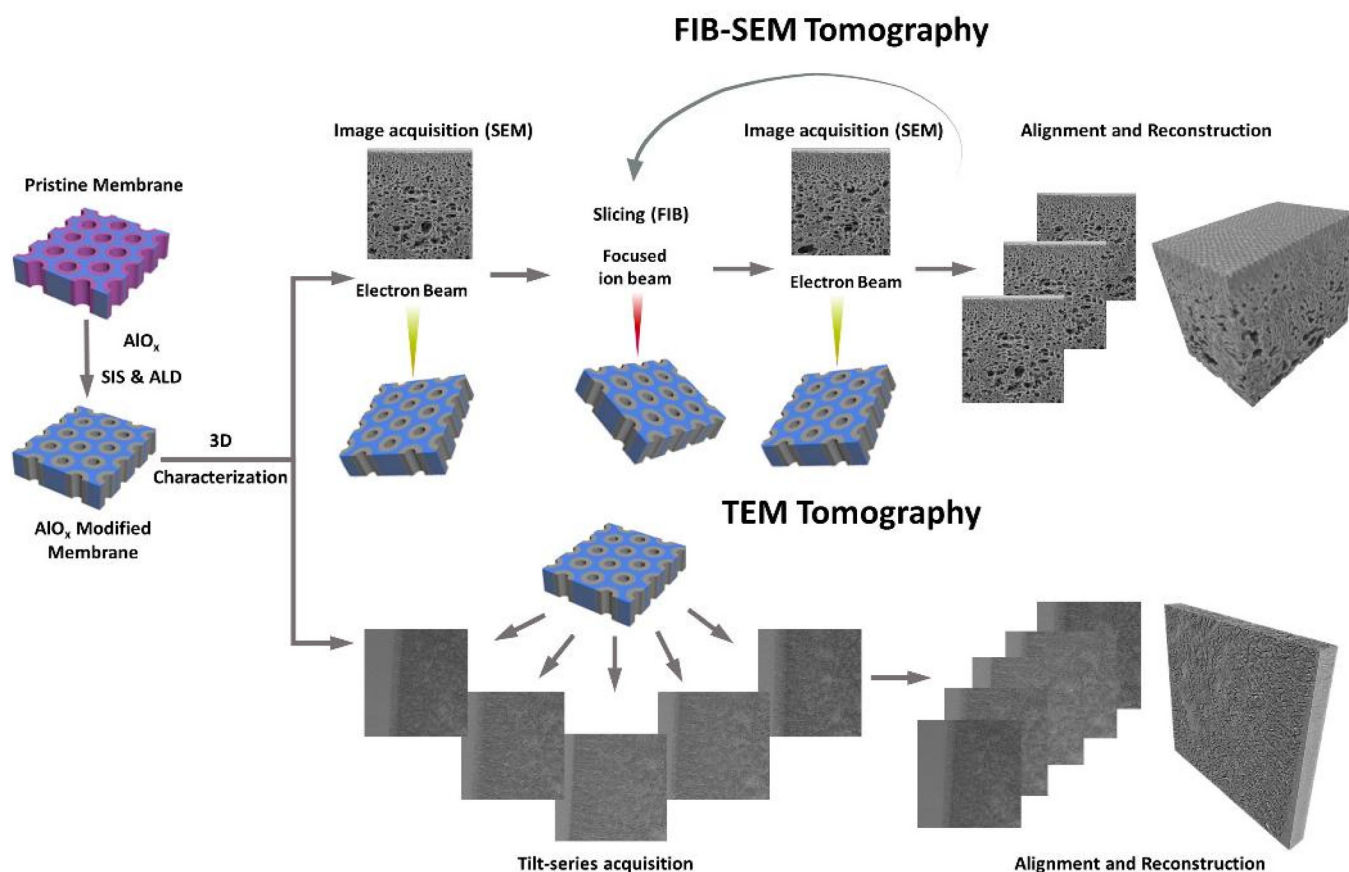


**Fig. 2** Illustration of the 3D characterization process:  $\text{AlO}_x$  is selectively grown in the P4VP pore-forming domain by SIS, followed by additional cycles of  $\text{AlO}_x$  ALD. This enhances the contrast, allowing for both FIB-SEM tomography and TEM tomography with high detail and resolution.

resulting pore network (Fig. 4d) visualizes the pores' location (blue spheres) and the connecting channels (gray cylinders). One should note that the membranes' surface connectivity (visualized by gray cylinders at the top of the membrane) is an artifact. However, since we are probing a large volume, this surface effect is negligible. The 3D pore network algorithm computes the effective absolute permeability  $k$  (in  $\mu\text{m}^2$ ) by analyzing the flow through the channels and the effective 3D tortuosity factor. Detailed information on how the algorithm computes all these parameters can be found in the ESI.†

To probe the correlation between the 3D pore structure and the membrane's macroscopic properties, we calculated the permeabilities of the overall structure (selective plus supporting layer) and the selective layer alone from the pore network 3D model and then compared them with the experimentally calculated permeability (Table 1). When the simulation was based on the selective layer alone, we observed a good agreement between the simulated permeability from the pore network 3D model and the experimental permeability (Table 1). The measured permeability is calculated from the permeance, taking into account the length of the selective layer (see the ESI for additional details†).<sup>7</sup> Thus, the good agreement supports the presumption that the selective layer is the bottleneck for flow. On the other hand, when we simulated the per-

meability of the entire 3D characterized volume, including the sub-structure, we obtained higher permeability values compared to the measured permeability while the flow rate in both layers was of the same order of magnitude (Table 1). These comparisons indicate that the selective layer mainly hinders the flow while the rather thick and tortuous 3D structure of the supporting layer has a negligible contribution to flow reduction. Importantly, this is the first time, to the best of our knowledge, that simulations from 3D characterization data provide insights into the relation between asymmetric membrane structures and the membrane's macroscopic properties.

One should note when calculating the permeability from the experimental data, we used the rough assumption that the selective layer has perfectly aligned cylinders with an ideal tortuosity factor of 1 (the tortuosity is defined as the deviation of a path (in our case, the pores) from a straight line). However, we observed a tortuosity factor of 1.29 from the pore network 3D model (Table 1), indicating that the pores are not perfectly aligned throughout the selective layer. Nonetheless, the good agreement between the calculated and the measured permeability implies that the selective layer tortuosity does not significantly reduce the permeability.

Overall, FIB-SEM tomography together with  $\text{AlO}_x$  staining provides unprecedented ability to probe the full 3D structure



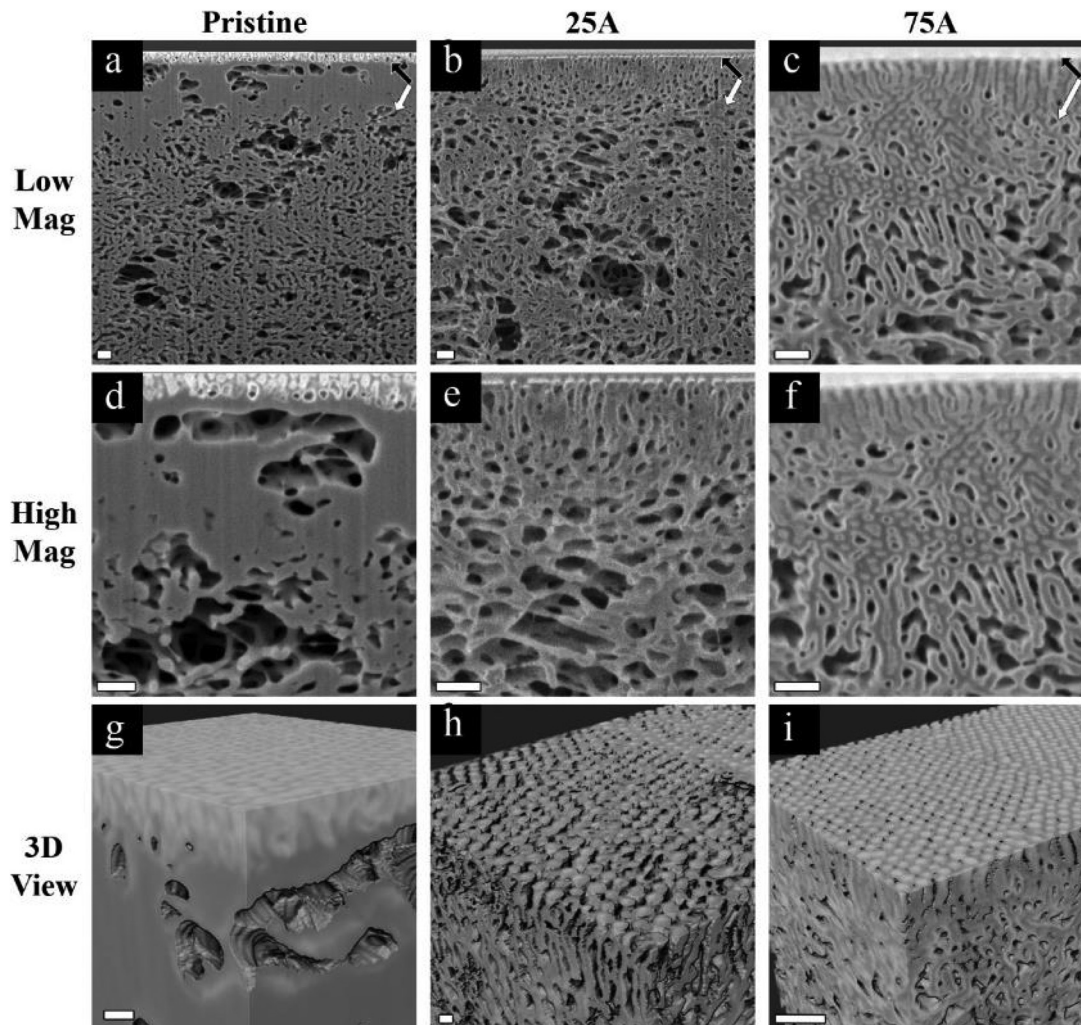


**Fig. 3** (a–f) Cross-sectional SEM images and (g–i) reconstructed 3D volume of pristine membrane (a, d and g) and membrane modified with 3 cycles of  $\text{AlO}_x$  SIS and 25 (b, e and h) or 75 cycles of  $\text{AlO}_x$  ALD (c, f and i). Images d–f are higher magnifications of images a–c, respectively. The black arrows point to the highly ordered selective layer and the white arrows to the underneath supporting layer. All the scale bars are 200 nm.

of the membranes and thus determine the significant role of the selective layer in the macroscopic properties. However, the requirements for resolving the selective layer and the substructure are at the limit of what can be achieved in FIB-SEM tomography runs, and hence small features in the selective layer are not well-resolved. Herein, we can bridge this gap by using TEM to achieve higher resolution for the selective layer. Thus, TEM tomography was performed as a complementary 3D characterization method to FIB-SEM tomography.

### TEM tomography

Based on the true-to-form and accurate staining of  $\text{AlO}_x$  in P4VP pore-forming domains as investigated in – FIB-SEM tomography section, we performed TEM tomography of 25A membranes and probed the ability to resolve the 3D structure of the ordered selective layer of the membrane.

The 3D volume reconstructed from the tomography tilt-series demonstrates the advantages of using TEM (Fig. 5a and b). The pores are more pronounced due to  $\text{AlO}_x$  growth (dark regions), and the high resolution provides higher levels of detail, compared to SEM (Fig. 3). The improved contrast between the blocks is visible over the depth of the pores with a high amount of detail. However, as discussed above, there is an inherent lack of contrast between the embedding material (epoxy resin) and the PS membrane matrix that hinders the ability to perform accurate segmentation. A demonstration of this effect can be seen in Fig. 5c and d. A selected slice from the 3D reconstructed volume (Fig. 5c) is segmented using a standard threshold algorithm and median filter (Fig. 5d). The segmented image shows that although  $\text{AlO}_x$  and hence the P4VP domains are clearly identified, the background epoxy and the PS region cannot be separated, reducing the ability to clearly resolve the BCP domains and the pores. Nonetheless, the 3D TEM tomography data enables unique 3D pore analysis.





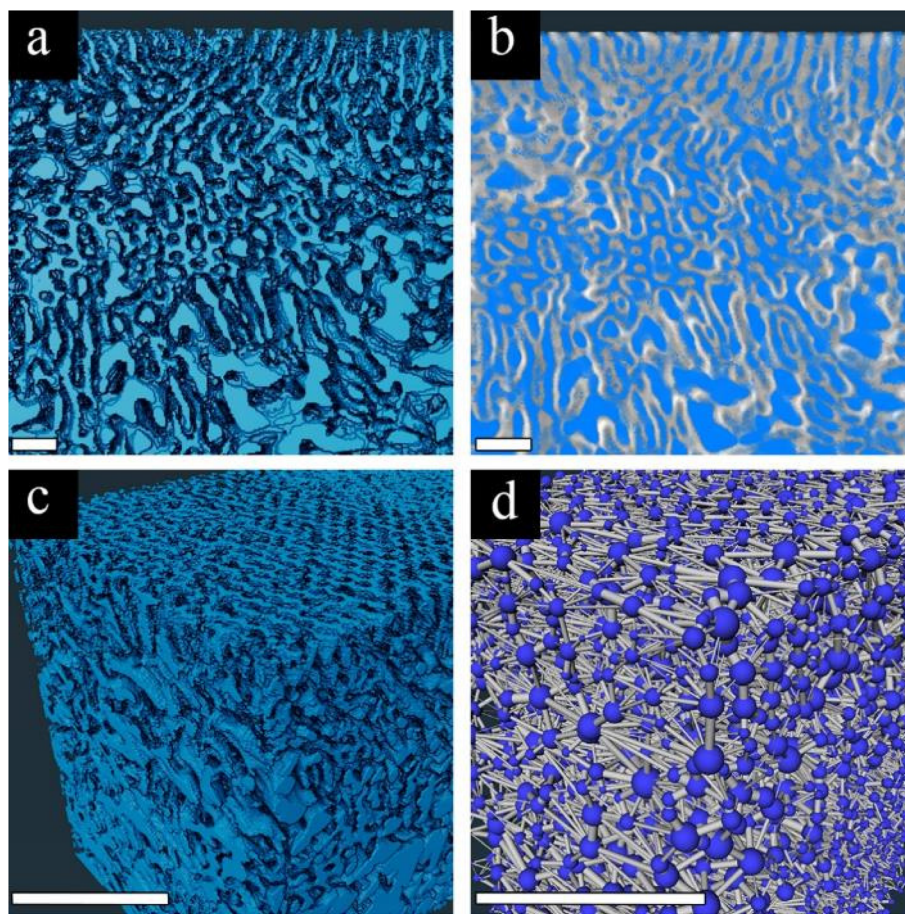


**Fig. 4** Segmentation of the FIB-SEM tomography 3D volume: (a) cross-sectional view of the segmented data, (b) segmentation overlaid with the original data, (c) 3D view of segmented data, and (d) 3D pore network reconstruction performed by using Amira. All the scale bars are 200 nm.

**Table 1** Results from pore network reconstruction simulation and experimentally measured data

Layer	Calculated from pore network 3D model			Experimental data Absolute permeability ( $k$ ) [ $\mu\text{m}^2$ ]
	Absolute permeability ( $k$ ) [ $\mu\text{m}^2$ ]	Total flow rate [ $\text{nm}^3 \text{s}^{-1}$ ]	Tortuosity ( $\tau$ )	
Selective	$3.33 \times 10^{-6}$	$2.51 \times 10^{12}$	1.29	$5.32 \times 10^{-6}$
Selective & Supporting	$3.27 \times 10^{-5}$	$1.73 \times 10^{12}$	1.74	—

With the 3D high-resolution data, several pore wall geometries can be identified in the top selective layer (Fig. 6a), including straight walls (blue arrow), curved walls (white arrow), and bent walls (black arrow). We focus on the pore morphology at the highly ordered selective layer, before the expansion to the supporting layer, as this area is the main hindrance to permeability, as discussed above. To quantitatively analyze the pores' structure throughout the reconstructed 3D volume, we classified four different pore-wall geometries: straight walls (S), single-side-bent walls (BL/BR for left or right wall bend, respectively), double-side inward bent walls (BLR), and curved walls (B). We followed the geometry of 13 different pores throughout the volume and plotted each pore's geometry *vs.* the perimeter of the pore, *i.e.* along the lateral direction of

the pore's axis (Fig. 6b shows an example for one pore, see the ESI for all profiles†).

Each geometry was assigned a penalty for deviation from a straight line, summarized in Table 2.

We arbitrarily chose a negative sign to denote both a right-hand side single wall bend and a double-wall inward bend, for visualization reasons only. This choice has no effect as we will look at the absolute value of the penalty for deviation. We assigned a penalty of 0.25 (positive or negative) for a single-wall bend, as we assume that its effect on flow is more minor than the other geometries. The penalty for double-sided bends (both inwards or curved) was set to 0.5 (positive or negative) as both hinder flow more drastically. Curved walls cause a longer residue time by elongating the path along the channel, while





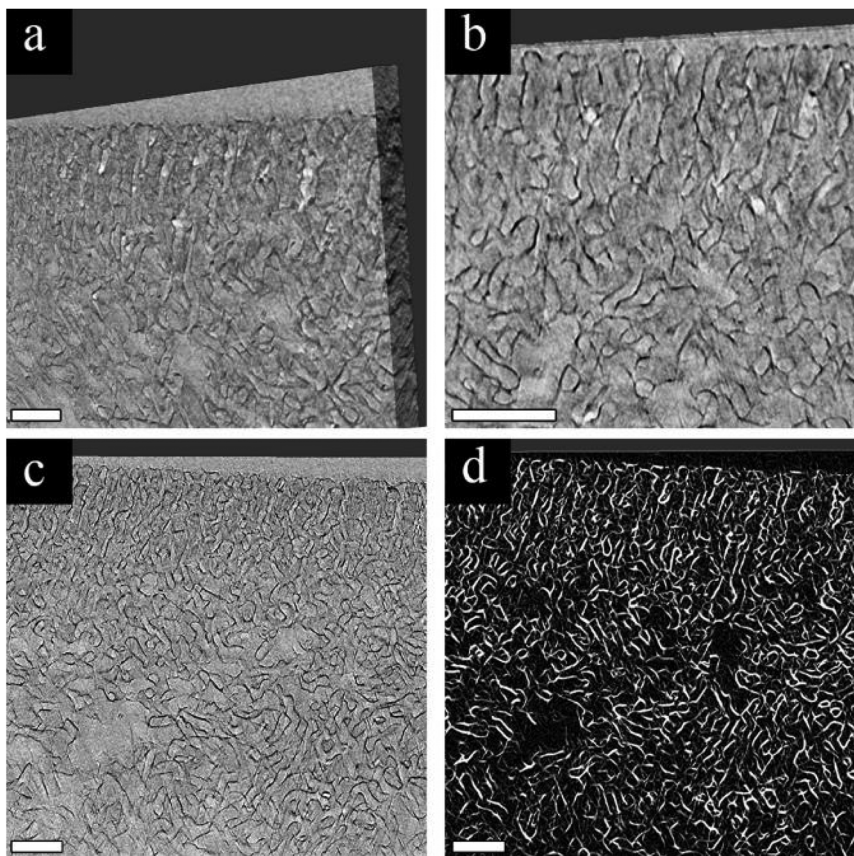


**Fig. 5** TEM tomography of the 25A membrane: (a–b) 3D view of the reconstructed volume at two magnifications, (c) a cross-sectional view from a selected slice, and (d) its segmentation. All the scale bars are 200 nm.

inward bent walls effectively reduce the pore diameter, causing a smaller mean-free path.

To evaluate the overall effect of the different pore geometries, we summed the absolute deviation penalty for each pore over the entire circumference of the pore and calculated each pore's deviation from a straight pore, a value we call the perimeter factor (PF), using the following equation:

$$\text{PF} = \% \text{deviation} = \frac{\sum_{i=1}^n |P_i - P(s)|}{n} \times 100\% \quad (1)$$

where  $P_i$  is the penalty for the current depth profile and  $P(s)$  is the penalty for a straight pore (in our case  $P(s) \equiv 0$ ). The results for all 13 pores and the histogram for their distribution are displayed in Fig. 6c and d, respectively. For example, if we look at pore no. 13 (visualized in Fig. 6b), initially we start with a straight pore (starting point is an 'S'), however, throughout the circumference of the pore, we can see some curving (rise to 'B') and some bending to the left-hand side (small ascent to 'BL') afterward, and finally, the pore seems to close (dip to a high negative number). This leads us to conclude that this pore's circumference is non-ideal, and flow through such a pore will highly deviate from ideal flux. This can be seen in Fig. 6c, where the PF of pore no. 13 is 32%. Such a deviation

can explain the lower permeability that was measured by FIB-SEM tomography for the selective layer. As the population of straight-walled pores decreases, the permeability should decrease, as either the path for flow is elongated or the effective area narrows down.

From these results, we observed an average deviation of 30% from a straight line. To our knowledge, this is one of the first times where the deviation from a straight line throughout a pore's 3D volume has been investigated. While deviation from a straight line differs from tortuosity, the PF can give us a further understanding of our pore's geometry in 3D and can play a factor in the overall membrane performance. As the separation mechanism is size based, if the channel's 3D nature is not completely straight, the residue time of the material going through each channel can vary within the membrane, affecting the effective overall permeance, selectivity, and local flow rate in the pores. Additionally, this deviation is in good agreement with the results from FIB-SEM tomography for the selective layer, where the tortuosity factor was 1.29. Therefore, we can postulate that the tortuosity factor and the 3D deviation are relatively similar and atone for similar flow effects. This shows the need for both FIB-SEM tomography and TEM tomography as complementary processes, one to probe the membrane structure and network, and the other to learn about the selective layer in more detail.



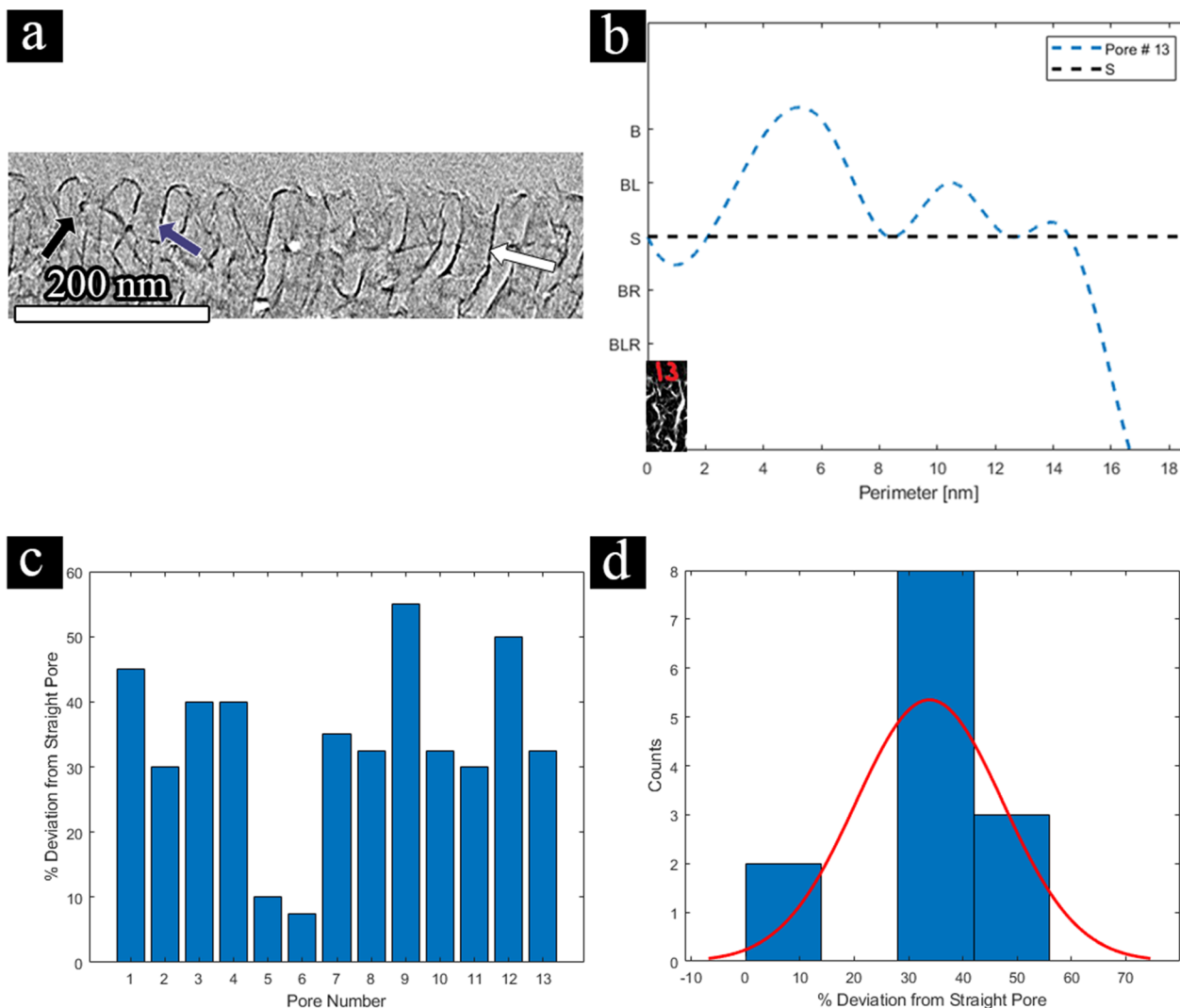


**Fig. 6** TEM tomography analysis – (a) selective slice from the TEM tomography 3D data; the white arrow shows a Double-Wall Curved Bend pore (B), the black arrow shows a Single-Wall Bend left pore (BL), and the blue arrow shows a Straight pore (S), (b) a perimeter profile of a single pore #13 at  $p=0$  nm (inset), (c) deviation from a straight pore for 13 selected pores, (d) a histogram of the deviation from a straight pore.

**Table 2** Penalty breakdown for deviation from a straight pore

Geometry	Illustration	Penalty for deviation from a straight line
Straight (S)		0
Single-Wall Bend (BL/R)		L: 0.25 R: -0.25
Double-Wall Inward Bend (BLR)		-0.5
Double-Wall Curved Bend (B)		0.5

## Conclusion

We demonstrated the ability to probe the 3D structure of BCP membranes by incorporating  $\text{AlO}_x$  selectively in the pore-forming domains. This allowed for high-resolution analysis of the membrane pore network. We managed to combine FIB-SEM tomography and TEM tomography to characterize both the selective layer and the underlying support layer, allowing us to learn about the correlation of the membrane's structure–performance. We used pore network analysis to create a 3D model of our membrane. This model enabled us to calculate the permeability and 3D tortuosity factor, providing a clear relationship between the 3D structure and macroscopic properties. TEM tomography explained these results quantitatively by analyzing the pore geometry throughout the membrane 3D volume. We believe that these findings can allow for better design of high-performance ultrafiltration membranes, to fulfill diverse on-demand requirements.



## Conflicts of interest

The authors declare no conflict of interest.

## Acknowledgements

The authors would like to thank Ivonne Ternes for polymer synthesis, Maren Brinkmann and Silvio Neumann for polymer characterization, Martin Held and Erik Schneider for support in the membrane structure characterization, Sapir Lifshiz-Simon for the process illustration, and Carsten Waltenberg and Sebastian Schädler from Zeiss Microscopy Customer Center Europe (ZMCCE) in Oberkochen, Germany, for performing the FIB-SEM tomography characterization.

## References

- R. P. Schwarzenbach, B. I. Escher, K. Fenner, T. B. Hofstetter, C. A. Johnson, U. von Gunten and B. Wehrli, The Challenge of Micropollutants in Aquatic Systems, *Science*, 2006, **313**(5790), 1072–1077, DOI: [10.1126/science.1127291](https://doi.org/10.1126/science.1127291).
- J. G. Crespo and K. W. Böddeker, *Membrane Processes in Separation and Purification*, Springer, Dordrecht; London, 2011.
- A. G. Fane, R. Wang and M. X. Hu, Synthetic Membranes for Water Purification: Status and Future, *Angew. Chem., Int. Ed.*, 2015, **54**(11), 3368–3386, DOI: [10.1002/anie.201409783](https://doi.org/10.1002/anie.201409783).
- D. M. Warsinger, S. Chakraborty, E. W. Tow, M. H. Plumlee, C. Bellona, S. Loutatidou, L. Karimi, A. M. Mikelonis, A. Achilli, A. Ghassemi, L. P. Padhye, S. A. Snyder, S. Curcio, C. D. Vecitis, H. A. Arafat and J. H. Lienhard, A Review of Polymeric Membranes and Processes for Potable Water Reuse, *Prog. Polym. Sci.*, 2018, **81**, 209–237, DOI: [10.1016/j.progpolymsci.2018.01.004](https://doi.org/10.1016/j.progpolymsci.2018.01.004).
- A. Lee, J. W. Elam and S. B. Darling, Membrane Materials for Water Purification: Design, Development, and Application, *Environ. Sci.: Water Res. Technol.*, 2016, **2**(1), 17–42, DOI: [10.1039/C5EW00159E](https://doi.org/10.1039/C5EW00159E).
- J. R. Werber, C. O. Osuji and M. Elimelech, Materials for Next-Generation Desalination and Water Purification Membranes, *Nat. Rev. Mater.*, 2016, **1**(5), 1–15, DOI: [10.1038/natrevmats.2016.18](https://doi.org/10.1038/natrevmats.2016.18).
- K.-V. Peinemann, V. Abetz and P. F. W. Simon, Asymmetric Superstructure Formed in a Block Copolymer via Phase Separation, *Nat. Mater.*, 2007, **6**(12), 992–996, DOI: [10.1038/nmat2038](https://doi.org/10.1038/nmat2038).
- V. Abetz, Isoporous Block Copolymer Membranes, *Macromol. Rapid Commun.*, 2015, **36**(1), 10–22, DOI: [10.1002/marc.201400556](https://doi.org/10.1002/marc.201400556).
- N. Hampu, J. R. Werber, W. Y. Chan, E. C. Feinberg and M. A. Hillmyer, Next-Generation Ultrafiltration Membranes Enabled by Block Polymers, *ACS Nano*, 2020, **14**(12), 16446–16471, DOI: [10.1021/acsnano.0c07883](https://doi.org/10.1021/acsnano.0c07883).
- J. Hahn, V. Filiz, S. Rangou, B. Lademann, K. Buhr, J. I. Clodt, A. Jung, C. Abetz and V. Abetz, PtBS-b-P4VP and PTMSS-b-P4VP Isoporous Integral-Asymmetric Membranes with High Thermal and Chemical Stability, *Macromol. Mater. Eng.*, 2013, **298**(12), 1315–1321, DOI: [10.1002/mame.201300012](https://doi.org/10.1002/mame.201300012).
- Z. Zhang, M. M. Rahman, C. Abetz and V. Abetz, High-Performance Asymmetric Isoporous Nanocomposite Membranes with Chemically-Tailored Amphiphilic Nanochannels, *J. Mater. Chem. A*, 2020, **8**(19), 9554–9566, DOI: [10.1039/D0TA01023E](https://doi.org/10.1039/D0TA01023E).
- K. Foroutani, S. M. Ghasemi and B. Pourabbas, Molecular Tailoring of Polystyrene-Block-Poly (Acrylic Acid) Block Copolymer toward Additive-Free Asymmetric Isoporous Membranes via SNIPS, *J. Membr. Sci.*, 2021, **623**, 119099, DOI: [10.1016/j.memsci.2021.119099](https://doi.org/10.1016/j.memsci.2021.119099).
- H. Yu, X. Qiu, N. Moreno, Z. Ma, V. M. Calo, S. P. Nunes and K.-V. Peinemann, Self-Assembled Asymmetric Block Copolymer Membranes: Bridging the Gap from Ultra- to Nanofiltration, *Angew. Chem., Int. Ed.*, 2015, **54**(47), 13937–13941, DOI: [10.1002/anie.201505663](https://doi.org/10.1002/anie.201505663).
- S. Schöttner, H.-J. Schaffrath and M. Gallei, Poly(2-Hydroxyethyl Methacrylate)-Based Amphiphilic Block Copolymers for High Water Flux Membranes and Ceramic Templates, *Macromolecules*, 2016, **49**(19), 7286–7295, DOI: [10.1021/acs.macromol.6b01803](https://doi.org/10.1021/acs.macromol.6b01803).
- R. M. Dorin, H. Sai and U. Wiesner, Hierarchically Porous Materials from Block Copolymers, *Chem. Mater.*, 2014, **26**(1), 339–347, DOI: [10.1021/cm4024056](https://doi.org/10.1021/cm4024056).
- W. A. Phillip, R. M. Dorin, J. Werner, E. M. V. Hoek, U. Wiesner and M. Elimelech, Tuning Structure and Properties of Graded Triblock Terpolymer-Based Mesoporous and Hybrid Films, *Nano Lett.*, 2011, **11**(7), 2892–2900, DOI: [10.1021/nl2013554](https://doi.org/10.1021/nl2013554).
- M. Radjabian and V. Abetz, Tailored Pore Sizes in Integral Asymmetric Membranes Formed by Blends of Block Copolymers, *Adv. Mater.*, 2014, **27**(2), 352–355, DOI: [10.1002/adma.201404309](https://doi.org/10.1002/adma.201404309).
- C. Yang, G. Zhu, Z. Yi, Y. Qiu, L. Liu and C. Gao, Tailoring the Pore Size and Permeability of Isoporous Membranes through Blending with Poly(Ethylene Glycol): Toward the Balance of Macro- and Microphase Separation, *J. Membr. Sci.*, 2020, **598**, 117755, DOI: [10.1016/j.memsci.2019.117755](https://doi.org/10.1016/j.memsci.2019.117755).
- Z. Zhang, M. M. Rahman, B. Bajer, N. Scharnagl and V. Abetz, Highly Selective Isoporous Block Copolymer Membranes with Tunable Polyelectrolyte Brushes in Soft Nanochannels, *J. Membr. Sci.*, 2022, **646**, 120266, DOI: [10.1016/j.memsci.2022.120266](https://doi.org/10.1016/j.memsci.2022.120266).
- J. Wang, M. M. Rahman, C. Abetz and V. Abetz, Tuning the Size Selectivity of Isoporous Membranes for Protein Fractionation via Two Scalable Post Treatment Approaches, *J. Membr. Sci.*, 2020, **614**, 118535, DOI: [10.1016/j.memsci.2020.118535](https://doi.org/10.1016/j.memsci.2020.118535).





- 21 Z. Zhang, M. M. Rahman, C. Abetz, A.-L. Höhme, E. Sperling and V. Abetz, Chemically Tailored Multifunctional Asymmetric Isoporous Triblock Terpolymer Membranes for Selective Transport, *Adv. Mater.*, 2020, **32**(8), 1907014, DOI: [10.1002/adma.201907014](https://doi.org/10.1002/adma.201907014).
- 22 R. A. Mulvenna, J. L. Weidman, B. Jing, J. A. Pople, Y. Zhu, B. W. Boudouris and W. A. Phillip, Tunable Nanoporous Membranes with Chemically-Tailored Pore Walls from Triblock Polymer Templates, *J. Membr. Sci.*, 2014, **470**, 246–256, DOI: [10.1016/j.memsci.2014.07.021](https://doi.org/10.1016/j.memsci.2014.07.021).
- 23 S. Park, J.-Y. Wang, B. Kim, J. Xu and T. P. Russell, A Simple Route to Highly Oriented and Ordered Nanoporous Block Copolymer Templates, *ACS Nano*, 2008, **2**(4), 766–772, DOI: [10.1021/nn7004415](https://doi.org/10.1021/nn7004415).
- 24 H. Ahn, S. Park, S.-W. Kim, P. J. Yoo, D. Y. Ryu and T. P. Russell, Nanoporous Block Copolymer Membranes for Ultrafiltration: A Simple Approach to Size Tunability, *ACS Nano*, 2014, **8**(11), 11745–11752, DOI: [10.1021/nn505234v](https://doi.org/10.1021/nn505234v).
- 25 T. Itzhak, N. Segev-Mark, A. Simon, V. Abetz, G. Z. Ramon and T. Segal-Peretz, Atomic Layer Deposition for Gradient Surface Modification and Controlled Hydrophilization of Ultrafiltration Polymer Membranes, *ACS Appl. Mater. Interfaces*, 2021, **13**(13), 15591–15600, DOI: [10.1021/acsmi.0c23084](https://doi.org/10.1021/acsmi.0c23084).
- 26 S. Y. Yang, J. Park, J. Yoon, M. Ree, S. K. Jang and J. K. Kim, Virus Filtration Membranes Prepared from Nanoporous Block Copolymers with Good Dimensional Stability under High Pressures and Excellent Solvent Resistance, *Adv. Funct. Mater.*, 2008, **18**(9), 1371–1377, DOI: [10.1002/adfm.200700832](https://doi.org/10.1002/adfm.200700832).
- 27 J. M. Sheldon, The Fine-Structure of Ultrafiltration Membranes. I. Clean Membranes, *J. Membr. Sci.*, 1991, **62**(1), 75–86, DOI: [10.1016/0376-7388\(91\)85005-P](https://doi.org/10.1016/0376-7388(91)85005-P).
- 28 R. F. Egerton, Radiation Damage to Organic and Inorganic Specimens in the TEM, *Micron*, 2019, **119**, 72–87, DOI: [10.1016/j.micron.2019.01.005](https://doi.org/10.1016/j.micron.2019.01.005).
- 29 L. F. Drummy, J. Yang and D. C. Martin, Low-Voltage Electron Microscopy of Polymer and Organic Molecular Thin Films, *Ultramicroscopy*, 2004, **99**(4), 247–256, DOI: [10.1016/j.ultramic.2004.01.011](https://doi.org/10.1016/j.ultramic.2004.01.011).
- 30 J. P. Buban, Q. Ramasse, B. Gipson, N. D. Browning and H. Stahlberg, High-Resolution Low-Dose Scanning Transmission Electron Microscopy, *J. Electron Microsc.*, 2010, **59**(2), 103–112, DOI: [10.1093/jmicro/dfp052](https://doi.org/10.1093/jmicro/dfp052).
- 31 J. S. Trent, J. I. Scheinbeim and P. R. Couchman, Ruthenium Tetraoxide Staining of Polymers for Electron Microscopy, *Macromolecules*, 1983, **16**(4), 589–598, DOI: [10.1021/ma00238a021](https://doi.org/10.1021/ma00238a021).
- 32 R. Deng, S. Liu, J. Li, Y. Liao, J. Tao and J. Zhu, Mesoporous Block Copolymer Nanoparticles with Tailored Structures by Hydrogen-Bonding-Assisted Self-Assembly, *Adv. Mater.*, 2012, **24**(14), 1889–1893, DOI: [10.1002/adma.201200102](https://doi.org/10.1002/adma.201200102).
- 33 Problems Associated with the Electron Microscopy of Polymers. In *Electron Microscopy of Polymers*, ed. G. H. Michler, Springer Laboratory, Springer: Berlin, Heidelberg, 2008, pp. 175–183. DOI: [10.1007/978-3-540-36352-1\\_9](https://doi.org/10.1007/978-3-540-36352-1_9).
- 34 Z. Zhang, A. Simon, C. Abetz, M. Held, A.-L. Höhme, E. S. Schneider, T. Segal-Peretz and V. Abetz, Hybrid Organic–Inorganic–Organic Isoporous Membranes with Tunable Pore Sizes and Functionalities for Molecular Separation, *Adv. Mater.*, 2021, **33**(48), 2105251, DOI: [10.1002/adma.202105251](https://doi.org/10.1002/adma.202105251).
- 35 D. Berman, S. Guha, B. Lee, J. W. Elam, S. B. Darling and E. V. Shevchenko, Sequential Infiltration Synthesis for the Design of Low Refractive Index Surface Coatings with Controllable Thickness, *ACS Nano*, 2017, **11**(3), 2521–2530, DOI: [10.1021/acsnano.6b08361](https://doi.org/10.1021/acsnano.6b08361).
- 36 W. Bao, L. Zhao, H. Zhao, L. Su, X. Cai, B. Yi, Y. Zhang and J. Xie, Vapor Phase Infiltration of ZnO Quantum Dots for All-Solid-State PEO-Based Lithium Batteries, *Energy Storage Mater.*, 2021, **43**, 258–265, DOI: [10.1016/j.ensm.2021.09.010](https://doi.org/10.1016/j.ensm.2021.09.010).
- 37 C. Zhou, T. Segal-Peretz, M. E. Oruc, H. S. Suh, G. Wu and P. F. Nealey, Fabrication of Nanoporous Alumina Ultrafiltration Membrane with Tunable Pore Size Using Block Copolymer Templates, *Adv. Funct. Mater.*, 2017, **27**(34), 1701756, DOI: [10.1002/adfm.201701756](https://doi.org/10.1002/adfm.201701756).
- 38 R. Azoulay, N. Shomrat, I. Weisbord, G. Atiya and T. Segal-Peretz, Metal Oxide Heterostructure Array via Spatially Controlled-Growth within Block Copolymer Templates, *Small*, 2019, **15**(51), 1904657, DOI: [10.1002/smll.201904657](https://doi.org/10.1002/smll.201904657).
- 39 I. Weisbord, N. Shomrat, H. Moshe, A. Sosnik and T. Segal-Peretz, Nano Spray-Dried Block Copolymer Nanoparticles and Their Transformation into Hybrid and Inorganic Nanoparticles, *Adv. Funct. Mater.*, 2019, **30**(18), 1808932, DOI: [10.1002/adfm.201808932](https://doi.org/10.1002/adfm.201808932).
- 40 Q. Peng, Y.-C. Tseng, S. B. Darling and J. W. Elam, A Route to Nanoscopic Materials via Sequential Infiltration Synthesis on Block Copolymer Templates, *ACS Nano*, 2011, **5**(6), 4600–4606, DOI: [10.1021/nn2003234](https://doi.org/10.1021/nn2003234).

